Single anisotropic gap superconductivity and proximity effect in $PbTaSe_2$

Chao-Sheng Lian,[1] Chen Si,[2,*] and Wenhui Duan[3,4,5,†]

[1]*International Laboratory for Quantum Functional Materials of Henan, School of Physics and Microelectronics, Zhengzhou University, Zhengzhou 450001, China*

[2]*School of Materials Science and Engineering, Beihang University, Beijing 100191, China*

[3]*Department of Physics and State Key Laboratory of Low-Dimensional Quantum Physics, Tsinghua University, Beijing 100084, China*

[4]*Collaborative Innovation Center of Quantum Matter, Beijing 100084, China*

[5]*Institute for Advanced Study, Tsinghua University, Beijing 100084, China*

(Received 2 September 2019; revised manuscript received 25 November 2019; published 12 December 2019)

$PbTaSe_2$ is a noncentrosymmetric superconductor having topological Dirac surface states as shown by recent experiments. Here, we report calculations on bulk and few-layer $PbTaSe_2$ using the first-principles anisotropic Migdal-Eliashberg theory, to explore the nature of the superconducting gap and the surface-bulk proximity effect in this stoichiometric system. In bulk, the multiband Pb p/Ta d Fermi surface exhibits a single anisotropic full superconducting gap, with larger gap values appearing on in-plane orbitals that can couple effectively to the in-plane phonons. A Pb-terminated few-layer $PbTaSe_2$ is found to still have a single-anisotropic-gap feature, but its superconducting gap is evidently reduced relative to the bulk case. Comparison between our theoretical results and experimental tunneling data suggests a significant proximity-enhanced superconductivity on the realistic surface of $PbTaSe_2$. The present findings would apply to other same-structured $ABSe_2$ (A = Pb, Sn; B = Ta, Nb) and are crucial for studying topological superconductors and Majorana fermions in promising topological metals with intrinsic full-gap superconductivity.

DOI: 10.1103/PhysRevB.100.235420

I. INTRODUCTION

The discovery of superconductivity in topological systems has aroused great research interest in topological superconductors (TSCs) [1–3] that host exotic excitations such as Majorana fermions. Unlike chiral p-wave superconductors which rarely exist in nature, topological insulator (TI)/s-wave superconductor heterostructures and superconducting topological metals are now considered promising platforms for realizing TSCs. In these systems, topological surface states (TSSs) can host Cooper pairs and become superconducting through the proximity effect from bulk s-wave superconductivity [4,5]. One famous heterostructure system is $Bi_2Se_3/NbSe_2$ [6–8] where a helical pairing of Dirac surface states has been observed [7]. Examples for superconducting topological metals include carrier-doped TIs [9–11] and chemically stoichiometric β-Bi_2Pd [12–14] and $PbTaSe_2$ [15–18]. The latter two intrinsic superconductors possess the required TSSs at the Fermi level (E_F) as revealed recently by angle-resolved photoemission spectroscopy (ARPES) [13,17] and have great advantages over the heterostructures or doped systems in both material synthesis and control.

Among stoichiometric systems, $PbTaSe_2$ containing hexagonal Pb layers sandwiched by $TaSe_2$ layers has been the focus of current research because of its noncentrosymmetric structure. The asymmetric spin-orbit coupling (SOC) can lift spin degeneracy, allowing a singlet-triplet mixed superconducting state [19–21]. Extensive works [22–27] have been done to probe the pairing symmetry of $PbTaSe_2$ which plays a crucial role in realizing its topological superconductivity. Specific heat [22], thermal conductivity [23], and London penetration depth [24] measurements consistently reveal a fully gapped superconducting state with no gapless nodes, but the accurate gap structure is still debated. While a multigap scenario was suggested from the upper critical field [22,25] and superfluid density [26] data, a single-gap BCS model described well the penetration depth data [24]. Moreover, a suppressed coherence peak below the superconducting critical temperature T_c in the nuclear spin-lattice relaxation rate might stem from either a single gap with anisotropy or multiple gaps [27]. It is thus critically important to determine the detailed superconducting gaps on the whole Fermi surface (FS) of bulk $PbTaSe_2$. On the other hand, the proximity-induced surface superconductivity [17] and how strong it is in $PbTaSe_2$ remain largely unexplored. A recent spectroscopic-imaging scanning tunneling microscopy (STM) study [28] has reported two spin-polarized Dirac TSSs on the Pb-terminated surface that can also be fully gapped at low temperature together with the bulk counterpart. However, in light of no well-defined interface existing between the bulk and surface states in stoichiometric $PbTaSe_2$, it is still difficult to experimentally separate their contributions to superconductivity in the tunneling spectrum. This calls for a complementary study of superconductivity in few-layer $PbTaSe_2$ to gain insight into the surface-bulk proximity effect in this intrinsic superconducting topological metal.

In this work, we elucidate from first-principles the nature of the superconducting gap and the pairing mechanism in

*sichen@buaa.edu.cn

†dwh@phys.tsinghua.edu.cn

both bulk and few-layer forms of $PbTaSe_2$ using the fully anisotropic Migdal-Eliashberg theory. This methodology has been applied to layered systems including the two-gap superconductor $2H$-NbS_2 [29]. Our results indicate that bulk $PbTaSe_2$ has a complicated multiband FS with mixed Pb p/Ta d orbital character and exhibits a strong electron-phonon coupling (EPC) anisotropy. It is revealed to be a phonon-mediated single-anisotropic-gap superconductor, with the superconducting pairing dominated by the low-energy Pb/Ta phonons. A two-dimensional (2D) Pb-$TaSe_2$-Pb few-layer system is found to have an evidently reduced superconducting gap relative to the bulk. Further comparative analysis with the STM data suggests a significant proximity-enhanced superconductivity in the surface layer of $PbTaSe_2$, enabling this superconducting system to be superior to the heterostructures for being immune to the complex interface interaction or the decaying pairing amplitude [7,30].

II. COMPUTATIONAL DETAILS

Density functional theory calculations are performed using the QUANTUM ESPRESSO package [31] with fully relativistic norm-conserving pseudopotentials [32,33]. The generalized gradient approximation of Perdew-Burke-Ernzerhof form [34] is adopted for the exchange-correlation functional. The plane-wave energy cutoff is set to 40 Ry. Bulk $PbTaSe_2$ crystallizes in a hexagonal lattice structure (space group $P\bar{6}m2$). To facilitate the comparison with experiments, we employ the experimental lattice constants ($a = 3.42$ Å and $c = 9.37$ Å) [28], with the atomic positions fully relaxed until the remanent forces are less than 0.001 eV/Å. An unshifted Brillouin-zone **k**-point mesh of $18 \times 18 \times 8$ and a Methfessel-Paxton smearing [35] of 0.02 Ry are adopted for the charge density calculations. The dynamical matrices and the linear variation of the self-consistent potential are computed within the framework of density functional perturbation theory [36] on a $6 \times 6 \times 2$ **q**-point mesh. The effects of SOC are included in the calculations of both the electronic structures and the phonon dispersions.

We employ the EPW code [37,38] to calculate the superconducting gap based on the anisotropic Migdal-Eliashberg theory [39,40]. The calculation of electronic wave functions required for Wannier-Fourier interpolation [37,41] within the EPW code is performed on a uniform unshifted **k**-point mesh of $12 \times 12 \times 4$. We use 14 maximally localized Wannier functions [42,43], three p states for each Pb (Se) atom, and five d states for the Ta atom to describe the electronic structure around E_F. The fully anisotropic Migdal-Eliashberg equations [40] are given by

$$Z(\mathbf{k}, i\omega_n) = 1 + \frac{\pi T}{N_F \omega_n} \sum_{\mathbf{k}'n'} \frac{\omega_{n'}}{\sqrt{\omega_{n'}^2 + \Delta^2(\mathbf{k}', i\omega_{n'})}} \times \delta(\epsilon_{\mathbf{k}'}) \lambda(\mathbf{k}, \mathbf{k}', n - n'), \quad (1)$$

$$Z(\mathbf{k}, i\omega_n)\Delta(\mathbf{k}, i\omega_n) = \frac{\pi T}{N_F} \sum_{\mathbf{k}'n'} \frac{\Delta(\mathbf{k}', i\omega_{n'})}{\sqrt{\omega_{n'}^2 + \Delta^2(\mathbf{k}', i\omega_{n'})}} \times \delta(\epsilon_{\mathbf{k}'})[\lambda(\mathbf{k}, \mathbf{k}', n - n') - \mu^*]. \quad (2)$$

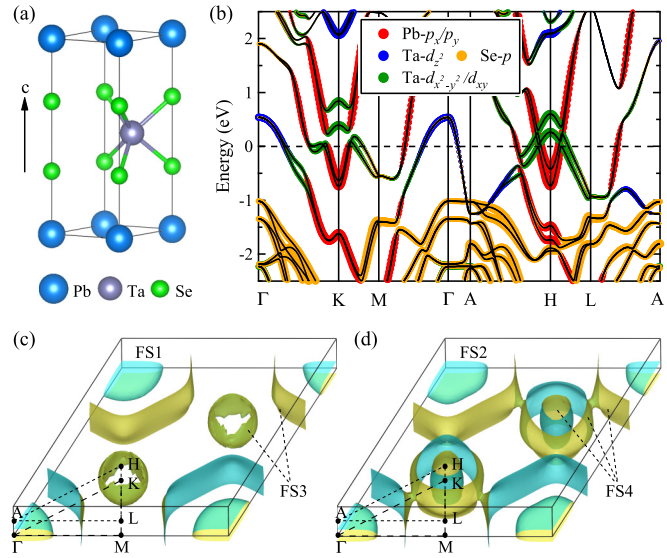

FIG. 1. (a) Crystal structure of $PbTaSe_2$. (b) Bulk electronic band structure under SOC. The red, blue, green, and orange dots represent the Pb p_x/p_y, Ta d_{z^2}, Ta $d_{x^2-y^2}/d_{xy}$, and Se p orbitals, respectively. (c, d) Bulk FS composed of the sheets FS1, FS2, FS3, and FS4 coming from the energy bands crossing the Fermi level in panel (b).

They form a coupled nonlinear system that needs to be solved self-consistently along the imaginary axis at the fermion Matsubara frequencies $\omega_n = (2n + 1)\pi T$ (n is integer) for each temperature T. Here, **k** (**k**′) indicates both the electron wave vector and the band index (note that the spin degeneracy of each state is lifted by SOC), $Z(\mathbf{k}, i\omega_n)$ is the mass renormalization function, $\Delta(\mathbf{k}, i\omega_n)$ is the superconducting gap function, μ^* is the semiempirical Coulomb parameter, and $\lambda(\mathbf{k}, \mathbf{k}', n - n')$ is the anisotropic EPC defined as [40]

$$\lambda(\mathbf{k}, \mathbf{k}', n - n') = N_F \sum_{\nu} \frac{2\omega_{\mathbf{q}\nu}}{(\omega_n - \omega_{n'})^2 + \omega_{\mathbf{q}\nu}^2} \left| g_{\mathbf{k}\mathbf{k}'}^{\nu} \right|^2. \quad (3)$$

In order to solve the Migdal-Eliashberg equations, we use grids containing $60 \times 60 \times 20$ **k** points and $30 \times 30 \times 10$ **q** points for bulk $PbTaSe_2$. The Matsubara frequency cutoff is set to ten times the maximum phonon frequency, and the Dirac deltas are replaced by Lorentzians of width 25 meV (electrons) and 0.05 meV (phonons). We have also calculated the superconducting properties of few-layer $PbTaSe_2$. The corresponding 2D film is simulated using a slab model with a vacuum thickness of 15 Å, and the charge density and dynamical matrices are computed using a 18×18 **k**-point mesh and a 6×6 **q**-point mesh, respectively. For the anisotropic Eliashberg equations we use 120×120 and 60×60 **k**- and **q**-point grids.

III. RESULTS AND DISCUSSIONS

A. Bulk electronic and phononic structures

$PbTaSe_2$ has a noncentrosymmetric hexagonal structure and consists of alternatively stacked Pb and $TaSe_2$ layers along the c direction [Fig. 1(a)]. The sublayer $TaSe_2$ is of the $1H$ form, corresponding to one monolayer of $2H$-$TaSe_2$. Figure 1(b) shows the bulk electronic band structure of

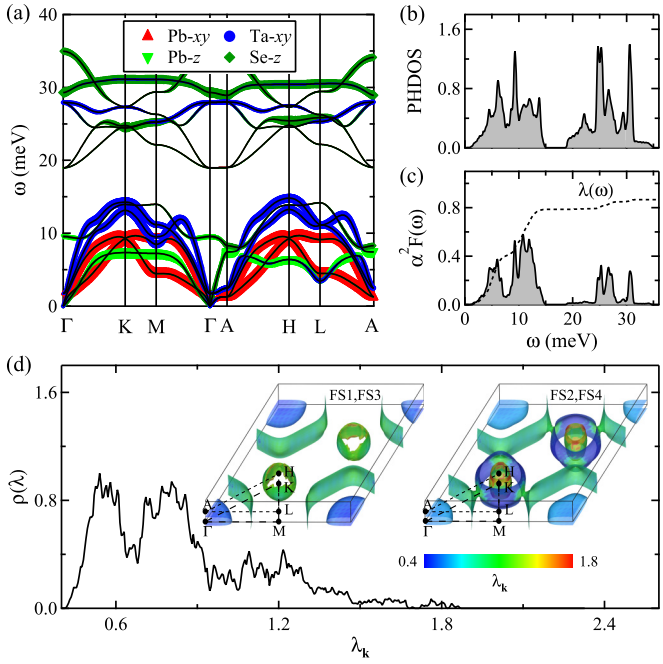

FIG. 2. (a) Phonon spectrum weighted by the vibration modes of different atoms, (b) PHDOS, and (c) isotropic Eliashberg spectral function $\alpha^2F(\omega)$ together with the cumulative EPC $\lambda(\omega)$ of bulk $PbTaSe_2$. (d) Distribution of the EPC strength $\lambda_{\mathbf{k}}$ by magnitude. Insets are the momentum-resolved EPC strength $\lambda_{\mathbf{k}}$ on the FS of $PbTaSe_2$.

$PbTaSe_2$ calculated with the inclusion of SOC, where the orbital contributions are proportional to the sizes of the colored dots. It is seen that $PbTaSe_2$ displays significant spin-orbit splitting due to the lack of inversion symmetry, resulting in complex energy bands around E_F and four FS sheets depicted in Figs. 1(c) and 1(d), in agreement with previous reports [16–18]. The two bands crossing the E_F around Γ form two three-dimensional (3D) hole pockets FS1 and FS2 centered at Γ. Both FS1 and FS2 originate from the $1H$-$TaSe_2$ sublayer and are of Ta d character with comparable out-of-plane d_{z^2} and in-plane $d_{x^2-y^2}/d_{xy}$ contributions. The higher-energy bands, on the other hand, form two composite FS sheets [FS3 and FS4 in Figs. 1(c) and 1(d)] because of the strong hybridization between Ta d and Pb p orbitals around E_F [Fig. 1(b)]. The sheet FS3 is composed of a quasi-2D hexagon-shaped cylinder around Γ and a toruslike hole pocket centered on the K-H (K'-H') line, both arising from mixed Ta $d_{x^2-y^2}/d_{xy}$ and Pb p_x/p_y states. The sheet FS4 is composed of a second hexagon-shaped cylinder around Γ, connected to a strongly corrugated subbranch around K (K'), and a pear-shaped cylinderlike electron pocket around the K-H (K'-H') line. Compared with FS3, the orbital feature of FS4 is more complex: while the Γ-centered hexagon-shaped cylinder is still of mixed in-plane Ta d/Pb p character, the K-centered outer corrugated subbranch arises from Ta $d_{x^2-y^2}/d_{xy}$ states mixed with Se p states; moreover, the electron pocket around K-H originates mainly from Pb p_x/p_y states with their corresponding weights along A-H-L ($k_z = \pi$) being larger than those along Γ-K-M ($k_z = 0$).

Figures 2(a) and 2(b) show the phonon spectrum and the phonon density of states (PHDOS) of $PbTaSe_2$. The $1H$-$TaSe_2$ sublayer is known to exhibit a charge-density wave (CDW) instability that results from a negative-energy phonon mode involving Ta xy vibrations [44,45]. In $PbTaSe_2$, the unstable $TaSe_2$ phonons are pushed upward due to the Pb intercalation which eliminates the CDW [17], and the low-energy phonons are contributed mostly by the vibrations of the heaviest Pb atoms [see Fig. 2(a)]. One can therefore identify three regions in the phonon spectrum associated with (i) the Pb-related modes (up to 10 meV), (ii) the Ta xy and Ta z modes (10–15 meV), and (iii) the Se-related modes (19–35 meV).

To quantify the interaction between electrons and phonons, the isotropic Eliashberg spectral function [40]

$$\alpha^2F(\omega) = \frac{1}{N_F N_{\mathbf{k}} N_{\mathbf{q}}} \sum_{\mathbf{k},\mathbf{k}',\nu} \left|g^{\nu}_{\mathbf{k}\mathbf{k}'}\right|^2 \delta(\epsilon_{\mathbf{k}})\delta(\epsilon_{\mathbf{k}'})\delta(\omega - \omega_{\mathbf{q}\nu}) \quad (4)$$

and the cumulative EPC $\lambda(\omega) = 2\int_0^{\omega} \alpha^2F(\omega')/\omega' d\omega'$ are calculated. In Eq. (4), N_F is the density of states per spin at E_F and $g^{\nu}_{\mathbf{k}\mathbf{k}'}$ represents the electron-phonon matrix element for the scattering between the electronic states $\mathbf{k}$ and $\mathbf{k}'$ through a phonon with wave vector $\mathbf{q} = \mathbf{k}' - \mathbf{k}$ and frequency $\omega_{\mathbf{q}\nu}$. As found in Fig. 2(c), the Pb modes below 10 meV and the Ta modes between 10 and 15 meV account for approximately 60% and 31% of the total coupling ($\lambda = 0.87$), respectively, whereas the Se modes above 19 meV have a small contribution of 9%. The total coupling of 0.87 computed here is larger than 0.66 reported in the previous work [17], probably owing to the electron-phonon Wannier interpolation used in this work. Further analysis of the coupling strength $\lambda_{\mathbf{q}\nu}$ of each phonon mode [see Fig. 6(a) in Appendix A] indicates it is the Pb xy and Ta xy modes that dominate the EPC in the low-energy regions, and the Pb z modes only show strong couplings when mixed with the Ta xy modes around L, while the Ta-z modes have little EPC contribution because of the reflection symmetry present in the $1H$-$TaSe_2$ sublayer [45–47]. Additionally, in the higher-energy region, considerable EPC arises from the coupled Ta-Se vibrations involving Ta xy modes [see Figs. 2(a) and 2(c)]. These facts suggest that in-plane Pb and Ta vibration modes, which can couple effectively to the Pb p or Ta d states around E_F, are mainly responsible for the electron-phonon interactions in $PbTaSe_2$.

We have also calculated the momentum-resolved EPC $\lambda_{\mathbf{k}}$ of each electronic state around E_F, defined as [40]

$$\lambda_{\mathbf{k}} = \sum_{\mathbf{k}',\nu} \delta(\epsilon_{\mathbf{k}'})\left|g^{\nu}_{\mathbf{k}\mathbf{k}'}\right|^2/\omega_{\mathbf{q}\nu}, \quad (5)$$

to evaluate the EPC anisotropy. Figure 2(d) plots the distribution of $\lambda_{\mathbf{k}}$ by magnitude. The obtained $\lambda_{\mathbf{k}}$ is seen to vary over the wide range 0.4–1.8, displaying a strong anisotropy. By examining its distribution on the FS in the insets of Fig. 2(d), we find obviously larger $\lambda_{\mathbf{k}}$ on FS3 and FS4 than on FS1 and FS2, except on the K-centered outer corrugated subbranch of FS4. In particular, the pear-shaped cylinderlike electron pocket of FS4 shows the largest $\lambda_{\mathbf{k}}$ near the A-H-L plane ($k_z = \pi$). Recalling the orbital analysis of different FS sheets in Fig. 1, it is recognized that the high $\lambda_{\mathbf{k}}$ values are sustained by the electronic states having predominant in-plane Ta d/Pb p character, whereas those states with component of Ta d_{z^2} or

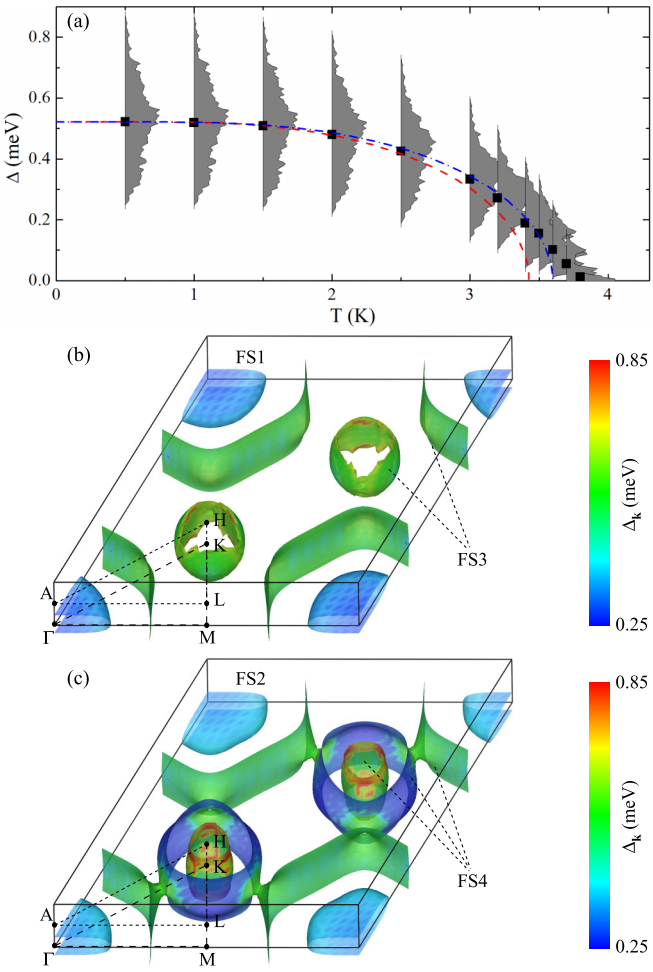

FIG. 3. (a) Energy distribution of the superconducting gap $\Delta_{\mathbf{k}}$ of bulk $PbTaSe_2$ as a function of temperature, calculated using the anisotropic Migdal-Eliashberg theory with a Coulomb pseudopotential μ^* of 0.15. The black squares indicate the average value of the gaps which vanishes at $T_c = 3.8$ K. The red dashed and blue dash-dotted lines are the BCS-model and α-model fittings to the calculated data, respectively. (b, c) Momentum-resolved superconducting gap $\Delta_{\mathbf{k}}$ on the FS of $PbTaSe_2$ at 0.5 K.

Se p character in general yield low $\lambda_{\mathbf{k}}$ values, consistent with the dominant role of in-plane Ta/Pb vibrations in the EPC.

B. Bulk superconducting properties

To clarify the superconducting pairing mechanism in bulk $PbTaSe_2$, we investigate its superconducting properties (gap function and critical temperature) by solving self-consistently the anisotropic Migdal-Eliashberg equations. Figure 3(a) shows the energy distribution of temperature-dependent superconducting gaps on the FS, calculated for a screened Coulomb pseudopotential $\mu^* = 0.15$, together with the average values of the gaps (black squares). Our results clearly indicate that $PbTaSe_2$ exhibits a single anisotropic superconducting gap with an average value of $\Delta_0 = 0.52$ meV in the zero-temperature limit, in good agreement with STM measurements [28] yielding $\Delta_0 = 0.45$ meV. The obtained gap structure is characterized by a relatively broad energy profile with a spread of 0.5 meV, which is comparable with the 0.34-meV spread found for another anisotropic single-gap superconductor β-Bi_2Pd [48]. Furthermore, the superconducting gap, as derived from Migdal-Eliashberg calculations, is seen to vanish at a critical temperature of $T_c = 3.8$ K, very close to the experimental data of 3.8 ± 0.2 K measured using different techniques [15,18,22–27].

We fit the data of the averaged superconducting gap versus temperature in Fig. 3(a) using a single-gap BCS model [49] and a single-gap α model [50] that extends the BCS theory by replacing $\alpha_{\mathrm{BCS}} = 1.764$ with an adjustable parameter $\alpha = \Delta_0/k_BT_c$. For the BCS model (red dashed line), the temperature dependence of Δ is obtained by solving numerically the gap function [49,51]

$$\int_0^{\frac{k_B\Theta_D}{\Delta_0}} \tanh\left(\frac{\alpha_{\mathrm{BCS}}\tilde{E}}{2t}\right)\frac{d\tilde{\varepsilon}}{\tilde{E}} = \ln\left[\frac{2k_B\Theta_D}{\Delta_0}\right], \tag{6}$$

with $t = T/T_c$, $\tilde{E} = \sqrt{\tilde{\varepsilon}^2 + \tilde{\Delta}^2}$ (being the reduced excited quasiparticle energy), $\tilde{\varepsilon} = \varepsilon/\Delta_0$, and $\tilde{\Delta} = \Delta/\Delta_0$, where Δ_0 is extracted from first-principles calculations and $k_B\Theta_D$ is the maximum phonon energy within the Debye theory set to $1000\Delta_0$ [48,51]. For the α-model (blue dash-dotted line), we obtain $\alpha = 1.68$ to yield the best fitting. Both fitting curves describe reasonably well the trend of the temperature-dependent superconducting gaps, though some deviations are seen around the critical temperature region. Overall, our calculated data are better fitted by the α-model with the parameter α of 1.68, in line with Δ_0/k_BT_c values of 1.70 and 1.75 as reported from the London penetration depth [24] and the nuclear spin-lattice relaxation rate [27] measurements, respectively.

In Figs. 3(b) and 3(c), we plot the momentum-resolved superconducting gap at 0.5 K on different sheets of the FS. We observe a finite value for $\Delta_{\mathbf{k}}$ at any position of the FS, indicating that the whole FS is gapped below the critical temperature. In particular, the distributions of $\Delta_{\mathbf{k}}$ on the Ta-dominated 3D hole pockets FS1 and FS2 (of mixed Ta d_{z^2} and $d_{x^2-y^2}/d_{xy}$) and on the sheet FS3 (of mixed Ta $d_{x^2-y^2}/d_{xy}$ and Pb p_x/p_y) are both nearly isotropic, with the gap values on FS1 and FS2 being close to the minimum of $\Delta_{\mathbf{k}}$ and those on FS3 centered around the average value of $\Delta_{\mathbf{k}}$. In sharp contrast, the gaps on the sheet FS4 are highly anisotropic and vary over the wide range 0.25–0.85 meV: the hexagon-shaped cylinder around Γ has a $\Delta_{\mathbf{k}}$ value close to that of FS3 due to their similar orbital character; the K-centered outer corrugated subbranch (of mixed Ta $d_{x^2-y^2}/d_{xy}$ and Se p) shows the smallest $\Delta_{\mathbf{k}}$ value; the pear-shaped cylinderlike electron pocket (of mainly Pb p_x/p_y) around K-H has a $\Delta_{\mathbf{k}}$ value higher than the average value, with the largest $\Delta_{\mathbf{k}}$ value appearing near the A-H-L plane ($k_z = \pi$). According to the above results, we conclude that large values of the superconducting gaps are on those regions of the FS composed of in-plane orbitals (Ta $d_{x^2-y^2}/d_{xy}$ and Pb p_x/p_y), while low values correspond to the regions with significant out-of-plane Ta d_{z^2} or Se p components. Such a unique distribution of the superconducting gap coincides well with the variation of the EPC strength on the individual FS sheets shown in the insets of Fig. 2(d).

It is interesting to compare the superconducting gap structure of $2H$-NbS_2 revealed in a recent theoretical work by

Heil *et al.* [29] with that of $PbTaSe_2$ studied here. In Heil *et al.*'s work, the regions of the FS with in-plane Nb $d_{x^2-y^2}/d_{xy}$ character are found to yield higher gap values than those with out-of-plane Nb d_{z^2} or S p_z character, in line with the gap distribution feature discussed above for $PbTaSe_2$. However, unlike $2H$-NbS_2 displaying two-gap superconductivity, $PbTaSe_2$ is found to be a single-anisotropic-gap superconductor. This can be attributed to the difference in the distribution of their EPC strength. For $2H$-NbS_2, a large superconducting gap, separated from another small gap in energy, originates from the electron-phonon hot spots on specific sizable FS regions, which are created by low-energy anharmonic phonons that bear a latent CDW instability [29]. For $PbTaSe_2$, such electron-phonon hot spots, however, are absent due to the suppression of the CDW of $TaSe_2$ sublayer by Pb intercalation and the hybridization between Ta d and Pb p states near the FS, which therefore cannot yield a separated higher superconducting gap.

C. Superconductivity in few-layer $PbTaSe_2$

Recently, Guan *et al.* [28] reported experimental evidence for $PbTaSe_2$ as a strong candidate for a TSC. Using STM and quasiparticle scattering interference (QPI) imaging, they successfully uncovered the proximity-induced fully gapped superconducting Dirac surface states on the Pb-terminated surface. Since in stoichiometric $PbTaSe_2$ both the surface and the bulk states contribute to the measured tunneling current but no well-defined interface exists between them, how to separate their contributions to superconductivity remains elusive. In order to probe the intrinsic superconductivity in the surface layer of $PbTaSe_2$ and understand how it is affected by the surface-bulk proximity effect, in the following calculations, we consider a few-layer $PbTaSe_2$ system containing one $TaSe_2$ layer sandwiched between two Pb layers as depicted in Fig. 4(a), evaluate its electron-phonon and superconducting properties, and make a direct comparison with bulk $PbTaSe_2$.

The phonon spectrum, the PHDOS, the Eliashberg spectral function $\alpha^2F(\omega)$, and the cumulative EPC $\lambda(\omega)$ for few-layer $PbTaSe_2$ are plotted in Fig. 4(b). The absence of any imaginary modes clearly indicates the dynamical stability of this 2D Pb-$TaSe_2$-Pb system, in good agreement with Guan *et al.*'s studies [28] reporting that the Pb-terminated surface is stable and has no CDW signature revealed on the Se-terminated surface. Similar to the bulk case, the Pb vibrations dominate the low-energy phonons below 8 meV, while the phonons in the higher-energy regions of 8–15 and 19–32 meV arise from mainly the Ta and Se vibrations. The phonons in the above three regions account for 80%, 15%, and 5% of the total coupling ($\lambda = 0.59$), respectively. The total EPC value of 0.59 computed here for few-layer $PbTaSe_2$ is considerably smaller than the value of 0.87 for its bulk counterpart, implying a weakening of superconductivity (see below). By examining the mode-resolved EPC strength [see Fig. 6(b) in Appendix A], we find that electron-phonon interactions in the few-layer system are also dominated by in-plane Pb xy and Ta xy modes as in the bulk. However, different from bulk $PbTaSe_2$ where Pb z modes (except those around L) show little couplings with electrons, here Pb z modes around 5 meV in a sizable region surrounding K contribute to the EPC, which is

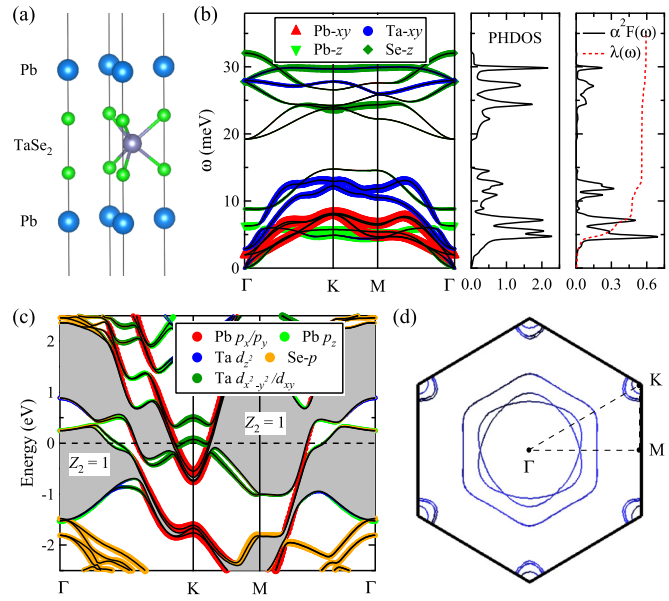

FIG. 4. Electron-phonon properties of few-layer $PbTaSe_2$. (a) Crystal structure with one $TaSe_2$ layer sandwiched between two Pb layers. (b) Phonon spectrum, PHDOS, isotropic Eliashberg spectral function $\alpha^2F(\omega)$, and the cumulative EPC $\lambda(\omega)$. (c) Electronic band structure weighted by the Pb p_x/p_y, Pb p_z, Ta d_{z^2}, Ta $d_{x^2-y^2}/d_{xy}$, and Se p orbitals. (d) The FS under SOC. The gray-shaded regions in panel (c) indicate the continuous energy gap below which the corresponding Z_2 invariant is computed.

ascribed to the breaking of local reflection symmetry at the Pb site and the emergence of Pb p_z states around E_F in few-layer $PbTaSe_2$.

The band structure and FS of few-layer $PbTaSe_2$ calculated under SOC are shown in Figs. 4(c) and 4(d). Among the energy bands crossing the E_F, the lowest two form two innermost hole pockets around Γ, which arise from Ta $d_{x^2-y^2}/d_{xy}$ states mixed with Pb p_z states instead of with Ta d_{z^2} states as for FS1 and FS2 in the bulk. The higher-energy bands each form a FS sheet centered at Γ or K (K'), exhibiting either Ta $d_{x^2-y^2}/d_{xy}$ or Pb p_x/p_y character. Figure 5(a) shows the energy distribution of the superconducting gap $\Delta_{\mathbf{k}}$ of few-layer $PbTaSe_2$ as a function of temperature. Similar to the bulk case, it also displays a single anisotropic superconducting gap featuring an energy profile with a spread of 0.23 meV. Analysis of the momentum-resolved $\Delta_{\mathbf{k}}$ indicates that large gap values appear on the FS sheets with in-plane Ta d/Pb p character, while those sheets with an out-of-plane Pb p_z component have low gap values, yielding an orbital-dependent gap distribution feature similar to that in the bulk. The average value of the gaps at zero temperature is estimated to be $\Delta_0 = 0.17$ meV, much smaller than the value of 0.52 meV calculated for bulk $PbTaSe_2$. Meanwhile, the superconducting gap vanishes at a rather low critical temperature of $T_c = 1.3$ K, compared to the bulk value of ~3.8 K. We notice that the nominal composition in the few-layer system is Pb_2TaSe_2, due to which the Fermi level could be shifted from the actual surface-layer case of $PbTaSe_2$. To test the sensitivity of our results to this effect, we repeated our Eliashberg calculations via changing the Fermi energy by up to ±100 meV. All the resulting T_c values are

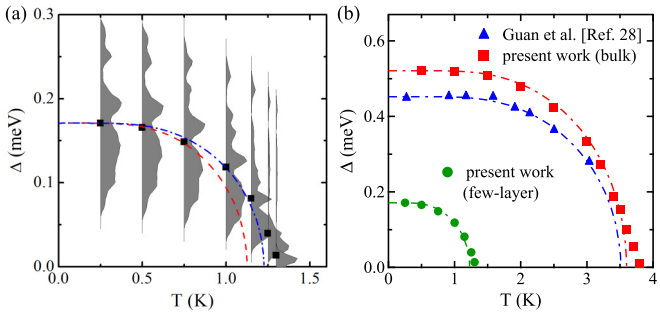

FIG. 5. (a) Energy distribution of temperature-dependent superconducting gaps of few-layer $PbTaSe_2$, calculated using the anisotropic Migdal-Eliashberg theory and $\mu^* = 0.15$. The average value of the gaps (black squares) vanishes at $T_c = 1.3$ K, with corresponding BCS-model (red dashed line) and α-model (blue dash-dotted line) fittings also plotted. (b) Comparison between theoretical and experimental [28] superconducting gaps. The theoretical data represent the average value of the gaps extracted from Figs. 3(a) and 5(a). The curves indicate the α-model fitting to the superconducting gap values.

found to be noticeably lower than in the bulk, confirming the weakening of superconductivity (see Fig. 7 in Appendix B).

We finally discuss the implication of our Migdal-Eliashberg results for understanding the superconducting proximity effect in $PbTaSe_2$. In Fig. 5(b) we plot the theoretical temperature-dependent superconducting gaps for both the bulk system and the few-layer system, together with available experimental STM data from Ref. [28]. Obviously, compared with the bulk, the superconducting order (the gap Δ_0 and critical temperature T_c) in the 2D Pb-$TaSe_2$-Pb system viewed as an isolated surface layer of $PbTaSe_2$ is weakened. However, in the tunneling spectrum taken on a realistic Pb-terminated surface, superconducting Δ_0 and T_c are observed to be close to those in the bulk. This sharp contrast indicates the surface layer of $PbTaSe_2$ may eventually exhibit a largely enhanced superconducting order relative to its fully isolated case as a consequence of the surface-bulk proximity effect. Though it is still necessary to simultaneously detect the surface and bulk gaps in future tunneling measurements with higher-energy resolution, our current calculations have suggested that the proximity-induced surface superconductivity can be particularly strong in a stoichiometric bulk superconductor. In the previous study [17], Dirac surface states of $PbTaSe_2$ have been confirmed by the Z_2 invariant analysis and ARPES. QPI imaging study by Guan *et al.* [28] further revealed their helical spin polarization nature. In the scenario of the proximity effect between bulk and surface states of a superconducting topological metal [17], spin-momentum-locked electrons on the TSSs can form a helical Cooper pairing and bound Majorana fermions in the vortices. Additionally, it is worth noting that our calculated full superconducting gap for few-layer $PbTaSe_2$ and the presence of topological nontrivial continuous gaps ($Z_2 = 1$) across E_F in its band structure [Fig. 4(c)] suggest the coexistence of full-gap superconductivity and topological edge states, making this film system, once achieved experimentally, a candidate for exploring 2D TSCs.

IV. CONCLUSIONS

In conclusion, we have studied electron-phonon interactions and the nature of the superconducting gap in bulk and few-layer $PbTaSe_2$ using the first-principles anisotropic Migdal-Eliashberg theory. We find a strong EPC anisotropy on the multiband FS of bulk $PbTaSe_2$ resulting in a single full superconducting gap with an orbital-dependent distribution feature. The in-plane Pb/Ta orbitals can bear gap values larger than those with out-of-plane components due to an effective coupling to in-plane Pb/Ta phonons which dominate the EPC. We further reveal the 2D Pb-$TaSe_2$-Pb system to be also a single-anisotropic-gap superconductor, but with smaller total EPC and superconducting gap compared to the bulk. Combined with the experiments, our theoretical results highlight the key role of the proximity effect in determining the significant superconductivity observed on the realistic surface of $PbTaSe_2$. Since all the same structured superconducting $ABSe_2$ (A = Pb, Sn; B = Ta, Nb) members show similar electronic and phononic properties [52], we expect other members of this $ABSe_2$ family to behave similarly to $PbTaSe_2$. The present work will provide useful implications for future studies of the intrinsic superconducting topological-metal-based TSCs, which are vital to realizing Majorana fermions.

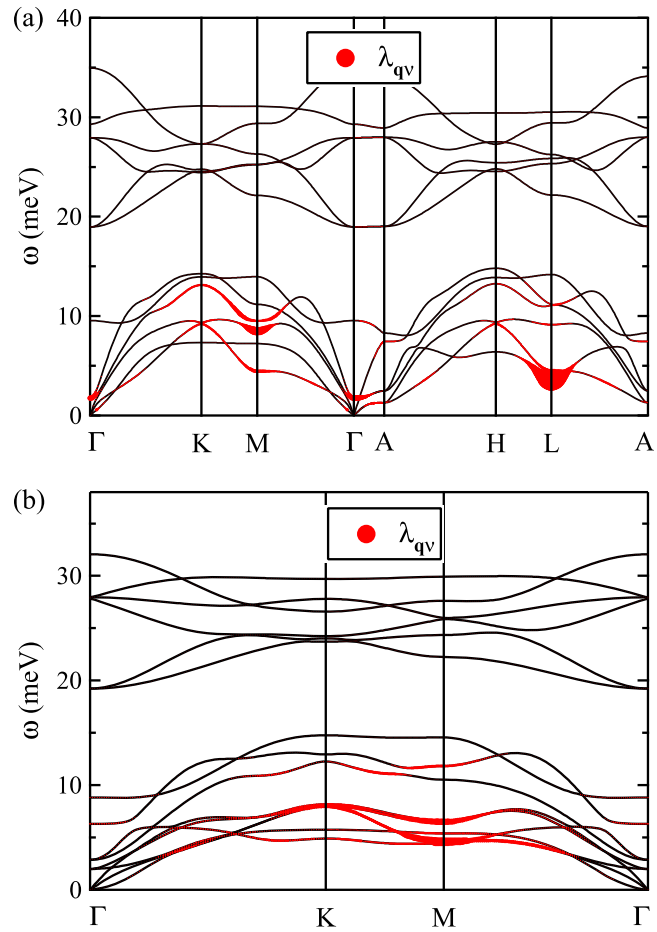

FIG. 6. Phonon spectra weighted by the mode-resolved EPC strength $\lambda_{\mathbf{q}\nu}$ of (a) bulk and (b) few-layer $PbTaSe_2$.

ACKNOWLEDGMENTS

This work was supported by the Ministry of Science and Technology of China (Grant No. 2016YFA0301001), the National Natural Science Foundation of China (Grants No. 11674188, No. 11874079, No. 11847116, and No. 51788104), and the Beijing Advanced Innovation Center for Future Chip (ICFC).

APPENDIX A: MODE-RESOLVED EPC STRENGTH $\lambda_{q\nu}$

Figure 6 shows the mode-resolved EPC strength $\lambda_{\mathbf{q}\nu}$ for both bulk and few-layer $PbTaSe_2$.

APPENDIX B: SENSITIVITY OF THE CALCULATED SUPERCONDUCTING PROPERTIES OF FEW-LAYER $PbTaSe_2$ TO THE FERMI ENERGY

In the main text, the nominal composition of Pb_2TaSe_2 in the few-layer system is different from $PbTaSe_2$ in the bulk, which could cause the Fermi energy to be shifted from the actual surface-layer case. To check this effect, we recalculated the Eliashberg equations with the Fermi level being raised or lowered by up to 100 meV. As shown in Fig. 7, the obtained T_c values vary in the range 0.8–2.3 K and remain evidently lower than the bulk value of ∼3.8 K. We have estimated the proper Fermi energy shift as −80 meV, based on a charge transfer of 0.16 electrons from one Pb layer to the remaining Pb-$TaSe_2$ subsystem as derived from Bader charge analysis and the Fermi level density of states of around 2 states/eV/cell. Correspondingly, for this Fermi energy shift we obtain $\Delta_0 = 0.27$ meV and $T_c = 2$ K, both values being smaller than those calculated for bulk $PbTaSe_2$. These results confirm that superconductivity in the isolated surface layer of $PbTaSe_2$ should be weakened relative to the bulk case.

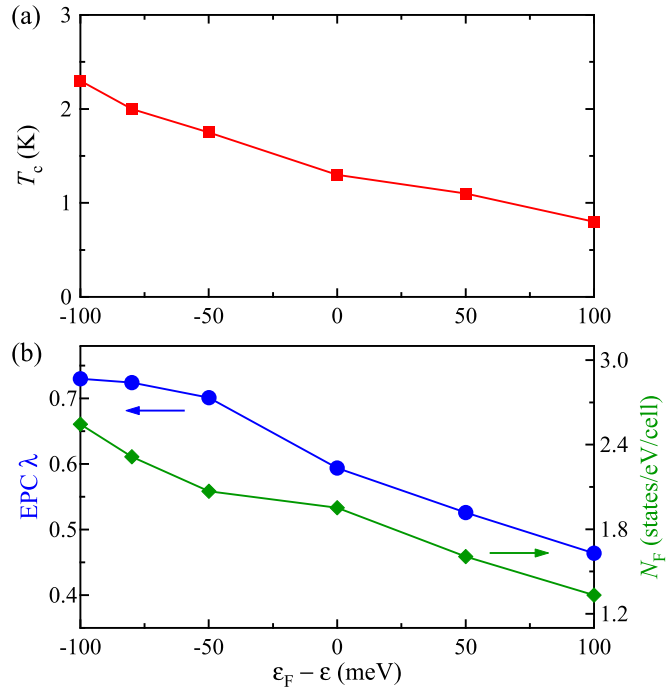

FIG. 7. (a) Variation of T_c calculated using the anisotropic Migdal-Eliashberg theory as a function of a rigid shift of the Fermi energy. (b) Variation of the EPC parameter λ and the Fermi level DOS N_F as a function of a rigid shift of the Fermi energy. Upon raising or lowering the Fermi level in the few-layer system by up to 100 meV, we obtain T_c to be always noticeably lower than ∼3.8 K in the bulk.

[1] M. Z. Hasan and C. L. Kane, Rev. Mod. Phys. **82**, 3045 (2010).
[2] X. L. Qi and S. C. Zhang, Rev. Mod. Phys. **83**, 1057 (2011).
[3] Y. Ando and L. Fu, Annu. Rev. Condens. Matter Phys. **6**, 361 (2015).
[4] P. Hosur, P. Ghaemi, R. S. K. Mong, and A. Vishwanath, Phys. Rev. Lett. **107**, 097001 (2011).
[5] L. Fu and C. L. Kane, Phys. Rev. Lett. **100**, 096407 (2008).
[6] M. X. Wang, C. H. Liu, J. P. Xu, F. Yang, L. Miao, M. Y. Yao, C. L. Gao, C. Y. Shen, X. C. Ma, Z. A. Xu *et al.*, Science **336**, 52 (2012).
[7] S. Y. Xu, N. Alidoust, I. Belopolski, A. Richardella, C. Liu, M. Neupane, G. Bian, S. H. Huang, R. Sankar, C. Fang *et al.*, Nat. Phys. **10**, 943 (2014).
[8] J. P. Xu, C. Liu, M. X. Wang, J. Ge, Z. L. Liu, X. Yang, Y. Chen, Y. Liu, Z. A. Xu, C. L. Gao, D. Qian, F. C. Zhang, and J. F. Jia, Phys. Rev. Lett. **112**, 217001 (2014).
[9] L. A. Wray, S. Y. Xu, Y. Xia, Y. S. Hor, D. Qian, A. V. Fedorov, H. Lin, A. Bansil, R. J. Cava, and M. Z. Hasan, Nat. Phys. **6**, 855 (2010).
[10] Y. S. Hor, A. J. Williams, J. G. Checkelsky, P. Roushan, J. Seo, Q. Xu, H. W. Zandbergen, A. Yazdani, N. P. Ong, and R. J. Cava, Phys. Rev. Lett. **104**, 057001 (2010).
[11] N. Levy, T. Zhang, J. Ha, F. Sharifi, A. A. Talin, Y. Kuk, and J. A. Stroscio, Phys. Rev. Lett. **110**, 117001 (2013).
[12] Y. Imai, F. Nabeshima, T. Yoshinaka, K. Miyatani, R. Kondo, S. Komiya, I. Tsukada, and A. Maeda, J. Phys. Soc. Jpn. **81**, 113708 (2012).
[13] M. Sakano, K. Okawa, M. Kanou, H. Sanjo, T. Okuda, T. Sasagawa, and K. Ishizaka, Nat. Commun. **6**, 8595 (2015).
[14] K. Iwaya, Y. Kohsaka, K. Okawa, T. Machida, M. S. Bahramy, T. Hanaguri, and T. Sasagawa, Nat. Commun. **8**, 976 (2017).
[15] M. N. Ali, Q. D. Gibson, T. Klimczuk, and R. J. Cava, Phys. Rev. B **89**, 020505(R) (2014).
[16] G. Bian, T. R. Chang, R. Sankar, S. Y. Xu, H. Zheng, T. Neupert, C. K. Chiu, S. M. Huang, G. Chang, I. Belopolski *et al.*, Nat. Commun. **7**, 10556 (2016).
[17] T. R. Chang, P. J. Chen, G. Bian, S. M. Huang, H. Zheng, T. Neupert, R. Sankar, S. Y. Xu, I. Belopolski, G. Chang *et al.*, Phys. Rev. B **93**, 245130 (2016).
[18] X. Xu, Z. Kang, T. R. Chang, H. Lin, G. Bian, Z. Yuan, Z. Qu, J. Zhang, and S. Jia, Phys. Rev. B **99**, 104516 (2019).
[19] R. P. Kaur, D. F. Agterberg, and M. Sigrist, Phys. Rev. Lett. **94**, 137002 (2005).

[20] E. Bauer and M. Sigrist, *Non-Centrosymmetric Superconductors: Introduction and Overview* (Springer, Berlin, 2012), Vol. 847.
[21] L. P. Gor'kov and E. I. Rashba, Phys. Rev. Lett. **87**, 037004 (2001).
[22] C. L. Zhang, Z. Yuan, G. Bian, S. Y. Xu, X. Zhang, M. Z. Hasan, and S. Jia, Phys. Rev. B **93**, 054520 (2016).
[23] M. X. Wang, Y. Xu, L. P. He, J. Zhang, X. C. Hong, P. L. Cai, Z. B. Wang, J. K. Dong, and S. Y. Li, Phys. Rev. B **93**, 020503(R) (2016).
[24] G. M. Pang, M. Smidman, L. X. Zhao, Y. F. Wang, Z. F. Weng, L. Q. Che, Y. Chen, X. Lu, G. F. Chen, and H. Q. Yuan, Phys. Rev. B **93**, 060506(R) (2016).
[25] J. Wang, X. Xu, N. Zhou, L. Li, X. Cao, J. Yang, Y. Li, C. Cao, J. Dai, J. Zhang, Z. Shi, B. Chen, and Z. Yang, J. Supercond. Novel Magn. **28**, 3173 (2015).
[26] M. N. Wilson, A. M. Hallas, Y. Cai, S. Guo, Z. Gong, R. Sankar, F. C. Chou, Y. J. Uemura, and G. M. Luke, Phys. Rev. B **95**, 224506 (2017).
[27] S. Maeda, K. Matano, and G. Q. Zheng, Phys. Rev. B **97**, 184510 (2018).
[28] S. Y. Guan, P. J. Chen, M. W. Chu, R. Sankar, F. Chou, H. T. Jeng, C. S. Chang, and T. M. Chuang, Sci. Adv. **2**, e1600894 (2016).
[29] C. Heil, S. Poncé, H. Lambert, M. Schlipf, E. R. Margine, and F. Giustino, Phys. Rev. Lett. **119**, 087003 (2017).
[30] C. K. Chiu, W. S. Cole, and S. Das Sarma, Phys. Rev. B **94**, 125304 (2016).
[31] P. Giannozzi, S. Baroni, N. Bonini, M. Calandra, R. Car, C. Cavazzoni, D. Ceresoli, G. L. Chiarotti, M. Cococcioni, I. Dabo *et al.*, J. Phys. Condens. Matter **21**, 395502 (2009).
[32] D. R. Hamann, Phys. Rev. B **88**, 085117 (2013).
[33] M. Schlipf and F. Gygi, Comput. Phys. Commun. **196**, 36 (2015).
[34] J. P. Perdew, K. Burke, and M. Ernzerhof, Phys. Rev. Lett. **77**, 3865 (1996).
[35] M. Methfessel and A. T. Paxton, Phys. Rev. B **40**, 3616 (1989).
[36] S. Baroni, S. de Gironcoli, A. D. Corso, and P. Giannozzi, Rev. Mod. Phys. **73**, 515 (2001).
[37] F. Giustino, M. L. Cohen, and S. G. Louie, Phys. Rev. B **76**, 165108 (2007).
[38] S. Poncé, E. R. Margine, C. Verdi, and F. Giustino, Comput. Phys. Commun. **209**, 116 (2016).
[39] P. B. Allen and B. Mitrović, Solid State Phys. **37**, 1 (1983).
[40] E. R. Margine and F. Giustino, Phys. Rev. B **87**, 024505 (2013).
[41] F. Giustino, Rev. Mod. Phys. **89**, 015003 (2017).
[42] N. Marzari, A. A. Mostofi, J. R. Yates, I. Souza, and D. Vanderbilt, Rev. Mod. Phys. **84**, 1419 (2012).
[43] A. A. Mostofi, J. R. Yates, Y. S. Lee, I. Souza, D. Vanderbilt, and N. Marzari, Comput. Phys. Commun. **178**, 685 (2008).
[44] H. Ryu, Y. Chen, H. Kim, H. Z. Tsai, S. Tang, J. Jiang, F. Liou, S. Kahn, C. Jia, A. A. Omrani *et al.*, Nano Lett. **18**, 689 (2018).
[45] C. S. Lian, C. Heil, X. Liu, C. Si, F. Giustino, and W. Duan, J. Phys. Chem. Lett. **10**, 4076 (2019).
[46] E. Mariani and F. von Oppen, Phys. Rev. Lett. **100**, 076801 (2008).
[47] C. Si, Z. Liu, W. Duan, and F. Liu, Phys. Rev. Lett. **111**, 196802 (2013).
[48] J. J. Zheng and E. R. Margine, Phys. Rev. B **95**, 014512 (2017).
[49] J. Bardeen, L. N. Cooper, and J. R. Schrieffer, Phys. Rev. **108**, 1175 (1957).
[50] H. Padamsee, J. E. Neighbor, and C. A. Shiffman, J. Low Temp. Phys. **12**, 387 (1973).
[51] D. C. Johnston, Supercond. Sci. Technol. **26**, 115011 (2013).
[52] P. J. Chen, T. R. Chang, and H. T. Jeng, Phys. Rev. B **94**, 165148 (2016).